Ultrasonics 133 (2023) 107027

Contents lists available at ScienceDirect

Ultrasonics

journal homepage: www.elsevier.com/locate/ultras

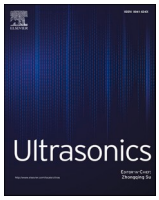

Elastic wave propagation in thick-walled hollow cylinders for damage localization through inner surface sensing

Yuanman Zhang [a,b,c], Shengbo Shan [d,*], Li Cheng [a,b,c,*]

[a] Department of Mechanical Engineering, The Hong Kong Polytechnic University, Kowloon, Hong Kong
[b] The Hong Kong Polytechnic University Shenzhen Research Institute, Shenzhen 518057, China
[c] Hong Kong Branch of National Rail Transit Electrification and Automation Engineering,Technology Research Center, The Hong Kong Polytechnic University, Kowloon, Hong Kong
[d] School of Aerospace Engineering and Applied Mechanics, Tongji University, Shanghai 200092, China

ARTICLE INFO

Keywords:
Quasi-surface-wave
Mode conversion
Damage localization
Thick-walled hollow cylinder

ABSTRACT

Thick-walled hollow cylinders (TWHCs) are widely used in engineering structures and transportation systems, exemplified by train axles. The real-time and online health monitoring of such structures is crucial to ensure their structural integrity and operational safety. While elastic-wave-based structural health monitoring (SHM) shows promise, the development of feasible methods strongly relies on a good understanding and exploitation of the wave propagation properties and their interaction with structural defects. TWHCs usually bear multiple wave modes, which is a less investigated and explored topic as compared with thin-walled structures. This work examines this issue and proposes a dedicated damage localization strategy by using the selected waves captured on the inner surface of a TWHC. It is shown that, alongside the quasi-surface-waves on the outer surface, longitudinal waves converted from the thickness-through shear bulk waves are generated to propagate along the inner surface. Their propagation characteristics are exploited for damage localization based on hyperbolic loci methods through inner surface sensing. Numerical studies are conducted to validate the method and assess different transducer configurations, alongside experimental verifications on a benchmark TWHC containing a notch-type defect. Studies provide guidance on damage detection in TWHCs and sensor network design.

1. Introduction

Thick-walled hollow cylinders (TWHCs) are widely used as major structural components in mechanical systems, exemplified by train axles [1–3]. During service, structural damages, such as cracks and corrosions, etc., can be initiated and evolve, which might jeopardize the safe operation of the system or even lead to catastrophic failure. Therefore, real-time and online monitoring of the occurrence of damage in such structures is crucial. Among existing techniques, structural health monitoring (SHM) based on ultrasonic guided waves holds great promise due to their appealing features such as high sensitivity to damage, large monitoring area, low energy consumption and so on [4–11].

Successful elastic-wave-based SHM techniques rely on a thorough understanding of the wave propagation in a given structure and its interaction with structural defects. Apart from a large amount of studies on thin plates in the context of guided waves, several investigations have also been carried out for hollow cylindrical structures. Analytical solutions on guided wave propagation in an infinitely long and hollow cylinder were first developed in the late 50s [12,13] for longitudinal [14–17], torsional[18–20] and flexural wave modes[21,22]. Although the proposed theoretical framework is applicable to both thin- and thick-walled hollow cylinders, subsequent studies mainly focused on the former due to the easier generation of pure guided wave modes and their relatively simple propagation pattern. For example, Eli *et al.* investigated the wave attenuation of the T(0,1) and L(0,2) guided wave modes in a pipe buried in sand[23]. Their study showed that the L(0,2) mode exhibits lower attenuation than T(0,1) mode. Sanderson *et al.* demonstrated the properties of torsional guided waves in pipe bends through finite element analyses[24], in which the effects of the wall thickness changes arising from the bending process were studied. Results indicated that the signals received beyond the pipe bend were not significantly affected[24]. Rose *et al.* explored the use of non-axisymmetric waves, especially flexural wave modes, for pipe inspection[25]. More

* Corresponding authors.
E-mail addresses: shanshengbo@tongji.edu.cn (S. Shan), li.cheng@polyu.edu.hk (L. Cheng).

https://doi.org/10.1016/j.ultras.2023.107027
Received 11 December 2022; Received in revised form 23 April 2023; Accepted 25 April 2023
Available online 29 April 2023

examples on guided wave as well as their application for the inspection of thin-walled pipes can be found in some review papers[26–30]. By comparison, wave propagation in TWHCs is much less exploited in the literature due to its increasing complexity and the coexistence of multiple mode types[31–33]. This typically occurs when the wall thickness approaches or exceeds the wavelength of the impinging waves. It is known that a surface excitation generates quasi-surface-waves with the wave energy confined mainly near the surface, similar to the surface waves in a half-infinite medium[34]. The phenomenon can be used to detect defects using sensors installed on the outer surface. For example, Ditri characterized a circumferential crack in hollow cylinders[35] with reflected/scattered quasi-surface-wave. A general theoretical framework was developed to analyze guided wave scattering with the S-parameter formalism. Aleksandra *et al.* detected a crack with the near-field wave enhancement effect using a sensor installed on the opposite surface to the quasi-surface-wave propagation surface based on the quasi-surface-wave interaction with the crack[36]. Li *et al.* detected the damage on the thick-walled train axle based on the mode conversion occurring at the quasi-surface interaction with the damage[32].

Compared with damage detection, damage localization in TWHCs is much more challenging, which has scarcely been addressed in the open literature. Among existing efforts on thin-walled cylinders, Hu *et al.* used an ellipse-based damage localization algorithm to locate damage in a pressure vessel based on an optimized sensor array[37]. Yang *et al.* proposed a real-time monitoring system for detecting and locating cracks in a storage vessel using guided wave with a developed discrete strategy[38]. However, these studies targeted thin-walled structures in which guided waves propagate in a relatively simple manner[39].

The above literature review demonstrates a lack of effort on the damage localization in TWHCs, which might be attributed to a two-fold reason: 1) lack of deep and thorough understanding of the propagation characteristics of different mode types inside a TWHC; and 2) insufficient effort on the exploration and synthetization of the wave features for damage localization. This forms the main motivation behind the present study. More specifically, this paper explores the propagation characteristics of different wave modes in a TWHC and, proposes a damage localization technique basd on inner inner sensing. Note sensing on the inner surface of a hollow cylinder is practically more attractive for engineering applications to avoid the harsh environement that outer suface exposes to. The rest of the paper is organized as follows. Guided wave theory and quasi-surface-waves in TWHCs are briefly recalled in Section 2, followed by an analysis using finite element simulations. Numerical simulations show different wave modes and their respective features. A damage localization strategy is then proposed by utilizing the sensing signals on the inner surface of the TWHC in Section 3. Based on the acquired understandings, numerical and experimental validations are carried out to demonstrate the efficacy of the proposed localization algorithm in Sections 4 and 5 respectively. Conclusions are finally drawn in Section 6.

2. Wave propagation in a thick-walled hollow cylinder

We consider the elastic wave propagation in a typical TWHC subjecting to a typical surface-traction excitation. For the completeness of the paper, basic theories of guided waves and quasi-surface-waves are briefly recalled. Analyses are carried out to illustrate the different wave propagation modes, along both surfaces and thickness-through direction, subject to an excitation applied on the outer surface of the TWHC. Based on these understandings, the wave packets in a typical time-domain response signal are identified with their corresponding wave components analysed.

2.1. Guided waves in a TWHC

Consider an isotropic hollow cylinder with an inner radius r_i and an outer radius r_o, for which a cylindrical coordinate system is defined in Fig. 1. The wave equation can be derived from Navier's equation as [12,13].

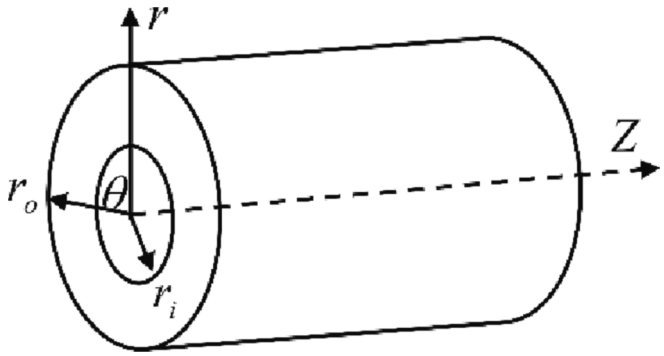

Fig. 1. Cylindrical-coordinate system assigned to an infinite cylinder.

$$\mu\nabla^2\boldsymbol{u} + (\lambda+\mu)\nabla\nabla\cdot\boldsymbol{u} = \rho\left(\partial^2\boldsymbol{u}/\partial t^2\right) \tag{1}$$

where $\boldsymbol{u}$ is the displacement vector; λ, μ denote the Lamé constants and ρ the mass density; ∇^2 is the three-dimensional Laplace operator. With the aid of Helmholtz decomposition, $\boldsymbol{u}$ can be decomposed into a dilatational scalar potential ϕ and an equivoluminal vector potential $\boldsymbol{H}$ as.

$$v_c^2\nabla^2\phi = \frac{\partial^2\phi}{\partial t^2} \tag{2}$$

$$v_s^2\nabla^2\mathrm{H} = \frac{\partial^2\mathrm{H}}{\partial t^2} \tag{3}$$

where v_c and v_s are the compressional and shear bulk wave velocities, respectively. Assuming a harmonic wave propagating in the z direction of the cylinder, the solutions to Eqs. (2) and (3) write.

$$\begin{aligned}
\phi &= f(r)cos(n\theta)e^{i(\xi z-\omega t)}\\
H_r &= h_r(r)sin(n\theta)e^{i(\xi z-\omega t)}\\
H_\theta &= h_\theta(r)cos(n\theta)e^{i(\xi z-\omega t)}\\
H_z &= h_z(r)sin(n\theta)e^{i(\xi z-\omega t)}.
\end{aligned} \tag{4}$$

where ξ and ω are the wavenumber and angular frequency, respectively; n refers to the circumferential mode order, which is equal to zero for axisymmetric modes and takes integer values from 1 to infinity for flexural modes. The functions f, h_r, h_θ, h_z describe the distribution of potentials ϕ and $\boldsymbol{H}$ in the radial direction.

The traction free boundary conditions $\sigma_{rr} = \sigma_{r\theta} = \sigma_{rz} = 0$ at the outer and the inner surfaces lead to a set of six homogeneous equations defining an eigenvalue problem. To achieve a non-trivial solution, the vanishing determinant condition has to be satisfied, resulting in the dispersion curves.

Guided waves in thick-walled hollow cylinders show complexe characteristics and can be divided into longitudinal, torsional, and flexural wave modes[21,35,40–42]. Under proper excitation, most guided-wave-based SHM techniques make use of high frequency range where various guided wave modes co-exist whose wavelengths are much smaller than the thickness of the hollow cylinder. Instead, quasi-surface-waves are more easily generated by the surface-mounted transducers in the TWHC, which hatches out the subsequent discussions on surface waves. Note Surface waves (also called Rayleigh waves) are rigorously defined in the literature as propagating guided waves along the free surface of a semi-infinite solid. They are non-dispersive and do not irradiate bulk waves toward the depth. As to be shown later in this paper, the waves propagating along the surface of the thick-walled hollow cylinders at high frequencies show the same characteristics as the surface waves in terms of the propagating speed, non-dispersive nature and wave structure. This can be easily understood physically, i.

e., as the wavelength of the surface wave at high frequencies is much smaller than the wall thickness of the cylinder, the cylinder can be roughly regarded as a semi-infinite medium. To discern the observed waves with the rigorously defined "surface waves" in the literature, we use the terminology "quasi-surface-waves" in the following discussion to show the similarity as well as the slight differences between the two types of waves.

2.2. Surface waves

Surface waves are theoretically formulated in a homogeneous, isotropic, linear elastic half-space with a free surface. Defining the wave propagation direction z and the thickness direction x and using the same Navier's equation as above, Helmholtz decomposition yields a dilatational wave and a rotational wave described by[43].

$$\nabla^2\varphi - \frac{1}{v_L^2}\ddot{\varphi} = 0 \text{ and } \nabla^2\vec{\psi} - \frac{1}{v_T^2}\ddot{\psi} = 0 \tag{5}$$

The solutions to this equation write $\varphi = A_1 e^{-kqx} e^{ik(z-ct)}$, $\psi = B_1 e^{-ksx} e^{ik(z-ct)}$, where the intermediate variables $q = \sqrt{1-\left(\frac{c}{v_L}\right)^2}$, $s = \sqrt{1-\left(\frac{c}{v_T}\right)^2}$ and c denotes the phase velocity of the surface wave. A_1, B_1 are the mode participation coefficients.

Upon applying the stress-free boundary conditions at the free surface, one has the dispersion relation of the surfaces waves as.

$$\eta^6 - 8\eta^4 + 8\eta^2\left(3 - 2\xi^2\right) + 16\left(\xi^2 - 1\right) = 0 \tag{6}$$

where.

$$\eta = \frac{k_T}{k} = \frac{c}{c_T}, \xi = \frac{k_L}{k_T} = \frac{c_T}{c_L} \tag{7}$$

It can be seen from Eq. (6) that the phase velocity of the surface waves is frequency independent, which means the surface waves are non-dispersive. In addition, the solutions to Eq. (8) give the approximate phase velocity of the surface waves[44] as.

$$c = \frac{(0.87 + 1.12\nu)}{(1+\nu)} c_T \tag{8}$$

where ν denotes the Poisson's ratio of the material.

2.3. Wave propagation induced by a surface-traction load

Consider the elastic wave propagation when a traction load is applied to the outer surface of a TWHC as illustrated in Fig. 2. The origin of the coordinate system is placed in the inner surface of the cross-section as shown below. The longitudinal and vertical directions of a TWHC correspond to z- and x-directions, respectively. When the excitation frequency is sufficiently high as the case in most SHM applications, the wavelength of multiple guided wave modes are much smaller than the wall thickness. A quasi-surface-wave is most likely to be generated and propagate on the outer surface of the TWHC. Meanwhile, by analyzing the partial vibration patterns, bulk shear waves are also generated to mainly propagate in the thickness direction along with some longitudinal wave components. When the bulk waves reach the inner surface, reflections and mode conversions occur, governed by the Snell's law. In this case, the dominant shear bulk waves are converted to longitudinal waves, propagating over the inner surface of the TWHC. This physical process is schematically illustrated in Fig. 2.

The predicted wave propagation process is confirmed by FE simulations. The FEM software used is ABAQUS/Explicit. The main parameters used in the simulations include: inner and outer radii of the hollow cylinder: 50 mm and 150 mm, respectively; Young's modulus of 71 GPa, mass density of 2700 kg/m3 and Poisson's ratio of 0.33. To simplify the analyses, two-dimensional models, shown in Fig. 3, are built to represent the two different cross-sections of the TWHC. As to be shown later, only the first arrivals in the signals are to be used for damage localization. Therefore, the cylinder length of 300 mm is enough to discern the first arrivals in the repsonse signals so that the reflections from the boundaries do not affect the proposed method. To mimic the surface excitation, a point-force, parallel to the top surface of the TWHC, is applied. The excitation signal is 5-cycle tone burst signal windowed by the Hann function at a central frequency of 300 kHz. To ensure the convergence and the accuracy of the simulation, the largest size of the mesh is set to 1 mm which ensures more than 10 elements per smallest wavelength under consideration. The sampling frequency is set to 10 MHz.

The resultant wave fields are obtained at 50 μs and displayed in Fig. 4, in terms of displacement magnitude. For the first case in Fig. 4(a) (cross-section along longitudinal direction), typical wave packets can be identified according to their respective propagating velocities and wavelengths. Specifically, strong waves are generated to propagate along the outer surface of the structure. Different from the rigorous definition of the surfaces waves for an infinitely large half space, the identified waves on the top surface on this thick structure are referred to as quasi-surface-waves whose propagating velocity is very close to idealized surface waves discussed in Section 2.2. As can be seen, the waves propagating along the surface of the thick-walled hollow cylinders at high frequencies show the same characteristics as the surface waves in terms of the propagating speed, non-dispersive nature and wave structure. Through the thickness direction, mainly shear bulk waves are generated. Interestingly, upon reaching the bottom surface, longitudinal waves appear along the inner surface rather than quasi-surface-waves, which will be discussed in the subsequent analyses.

For the case in Fig. 4(b) (cross-section along radial direction), typical

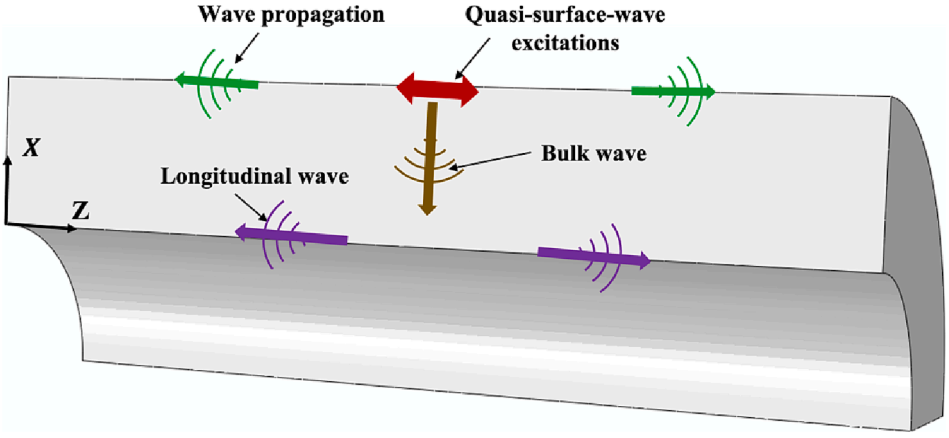

Fig. 2. Mode conversion on the inner surface.

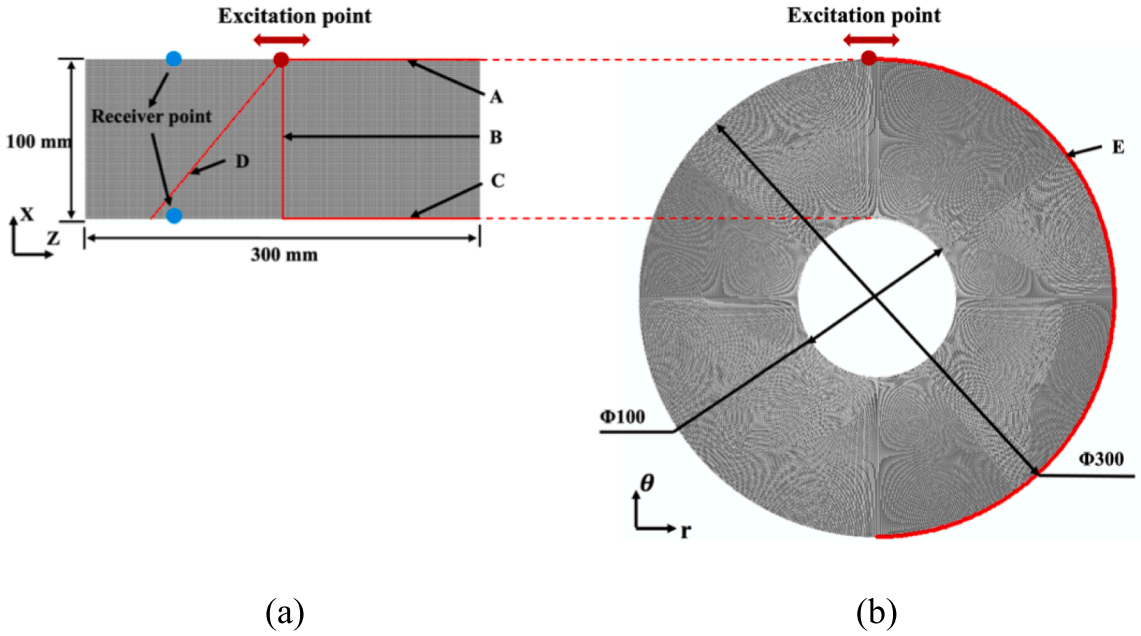

Fig. 3. Cylinder cross-section from (a) longitudinal direction, (b) radial direction.

wave packets can be identified according to wave propagation features along the circumferential direction. Though calculating the wave propagation velocity and observing the wave energy variation, results demonstrate that curvature does not sensibly affect the quasi-surface-wave propagation in the frequency range investigated in the paper, which lays out the foundation for further damage localization based on quasi-surface-waves.

To better visualize the wave propagation characteristics, different wave components propagating along different paths inside the structure (shown in Fig. 2) are extracted and plotted in Fig. 5 in terms of their respective displacement components, whose magnitudes are indicated by color. Along Path A on the upper/outer surface as shown in Fig. 5(a), two different waves can clearly be observed. Strong energy attenuation occurs at the first wave packet due to the evanescent nature of the waves. The second wave propagates without obvious attenuation at a constant phase velocity at around 2800 m/s, which is deduced from the slope of the wave trajectory. Two paths are selected along the thickness direction as Paths B and D. The wave propagation along Path B in the vertical thickness direction (x-direction), identified as shear wave, is displayed in Fig. 5(b) in terms of the z direction displacement. It propagates at a constant phase velocity at around 3066 m/s. Path D has an inclined angle of around 45°. The wave, with a strong x direction displacement, is identified as longitudinal wave, progapating at around 5400 m/s estimated according to the slope of the wave trajectory, as shown in Fig. 5(d). After the bulk waves reach the bottom/inner surface, mode conversion occurs, thus producing two propagating waves that are clearly observed as shown by the z-direction displacement field map along Path C, shown in Fig. 5(c). Through calculating their phase velocities and the time-of-flight, they are further identified as longitudinal waves, respectively. The wave propagation along Path E is illustrated in Fig. 5(e) in terms of radial direction displacement, which shows high similarity with that in Fig. 5(a) with pronounced quasi-surface-wave characteristics. The corresponding wave velocity is estimated to be 2800 m/s.

Based on the above observation, typical time-domain responses captured at specific positions can be explained. These information is of great help to iron out the subsequent damage localization methodology. For example, Fig. 6 shows the z direction displacement components at two representative sensing points on the top and bottom surfaces, corresponding to the blue points in Fig. 3(a). Identification of the corresponding wave packets suggests that the quasi-surface-wave dominates the response signal on the top surface (Fig. 6(a)). On the bottom surface, the longitudinal wave, converted by the shear bulk wave, shows much larger amplitude. Due to the large difference in the wave speeds between the longitudinal waves (5400 m/s) and the shear waves (3066 m/s), the detected longitudinal waves are mainly converted from the Path B instead of Path D. Therefore, the quasi-surface-wave on the top surface and longitudinal wave on the bottom surface are to be used for designing the subsequent damage localization method.

3. Damage localization scheme

In most practical situations, exemplified by a train axel, the outer surface of a TWHC is more vulnerable to damage due to the higher stress-level and direct exposure to the harsh environment. Based on the afore-acquired understanding on the wave propagation, a damage localization scheme based on hyperbolic method is proposed by exploiting the wave features captured on the inner surface of the TWHC. In addition, the sensor network arrangements are designed and evaluated from the perspective of localization accuracy.

3.1. Damage localization strategy

As illustrated in Fig. 7, two sets of transducer arrays are proposed to be installed on the outer and inner surfaces of a TWHC, respectively. While the former is used as the actuators on the outer surface, the deployment of the latter is to accommodate the need for more practical installation of the transducers.

In the proposed method, the sensors are installed on the inner surface of the hollow cylinder while the actuators are placed on the outer surface. Therefore, two coordinate systems are built on the inner and outer surfaces respectively as illustrated in Fig. 7(a) which are denoted as C1 and C2. They can be easily mapped through the radial direction as shown in Fig. 7(b). In this specific case, a sensor position (x, y) in C1 can be mapped to (x, 2y) in C2 considering the inner and outer radius of the hollow cylinder. As the proposed method makes use of the time difference of waves on the inner surface, damage localization is first carried out in C1. However, since damage is more likely to occur on the outer surface, the output image is reconstructed on C2 according to the mapping relation.

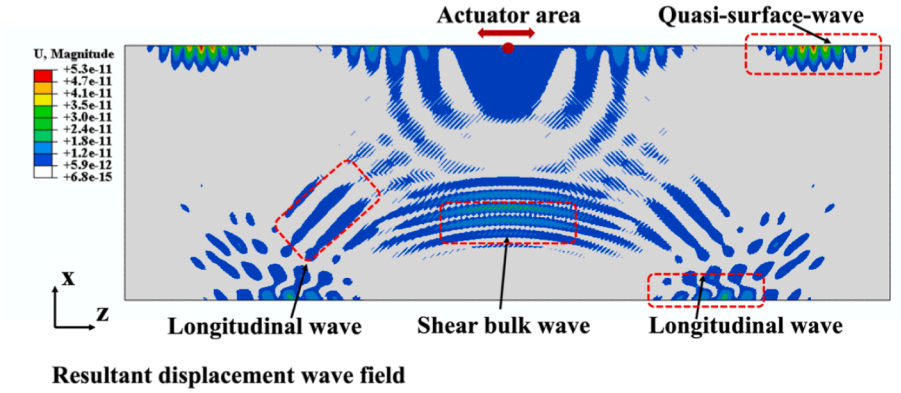

(a)

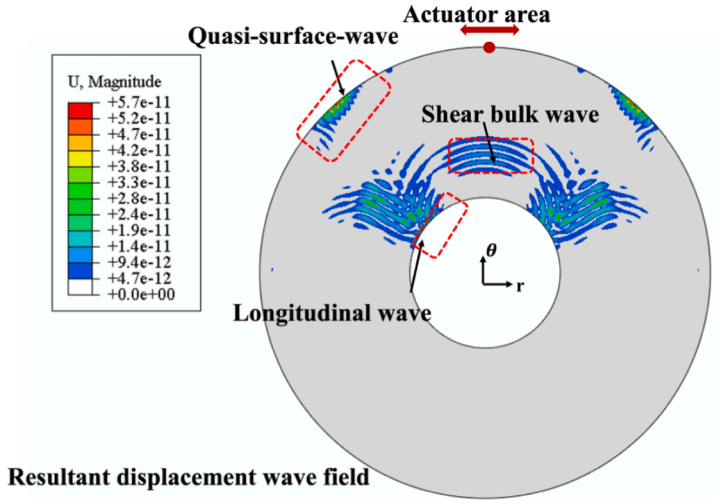

(b)

Fig. 4. FE simulated resultant wave displacement contours of wave propagation. (a) Wave propagation over the cross-section along longitudinal direction. (b) Wave propagation over the cross-section along radial direction.

In light of the revealed mode conversion on the inner surface, the hyperbolic loci method, often used for impact localization, is modified and applied with the sensor array on the inner surface of the TWHC. In this case, the outer surface transducers are used for wave excitation. When the quasi-surface-wave interacts with the damage on the outer surface, bulk waves are generated and propagate along the thickness direction. Once reaching the inner surface, the bulk waves are further converted to longitudinal waves, which propagate and are captured by different sensors installed over the inner surface. Therefore, the inner surface sensors can detect the signals originating from the damage and the external surface excitation.

For an arbitrary sensor pair s1 (x_{s1}, y_{s1})-s2 (x_{s2}, y_{s2}), the time difference of the damage-induced longitudinal waves can be obtained which is further related to the difference distance $D_{\text{d-crack}}$ from the damage(x_d, y_d) to the two sensors as.

$$D_{d-crack} = \left| \sqrt{(x_d - x_{s1})^2 + (y_d - y_{s1})^2} - \sqrt{(x_d - x_{s2})^2 + (y_d - y_{s2})^2} \right| = T_i \cdot v_{longitudinal} \tag{9}$$

where $v_{longitudinal}$ is the velocity of the longitudinal wave. T_i is the difference between the time-of-arrivals of the damage-induced waves reaching the two sensors. By the same token, if multiple sensor pairs are considered, the damage can be located by the intersection of their corresponding hyperbolas. The probability-based damage imaging philosophy is applied to obtain the possibility of damage occurrence at an arbitrary node $i(x, y)$ resulting from a specific sensor pair, which is defined as.

$$R_i(x, y) = 1 - \left| \frac{\left| D_{s1,i,s2} \right| - D_{d-crack}}{D_{s1,i,s2}} \right| \tag{10}$$

where $D_{s1,i,s2}$ is the difference between the distances from a specific node to the two sensors. By synthesizing the damage information from all sensor pairs, the overall possibility of damage occurrence at the node i can be obtained as.

$$p_{inner}(x, y) = \sum_{i=1}^{N} R_i(x, y) \tag{11}$$

Finally, a damage image can be further obtained by assessing all the nodes in the inspection area.

3.2. Evaluation of sensor network arrangement

The above proposed damage localization strategy requires a few spatially distributed transducers to be networked. Due to the sparsity of the sensors, a proper transducer network should be important to capture damage-related information while tolerating measurement uncertainties as well as measurement redundancy.

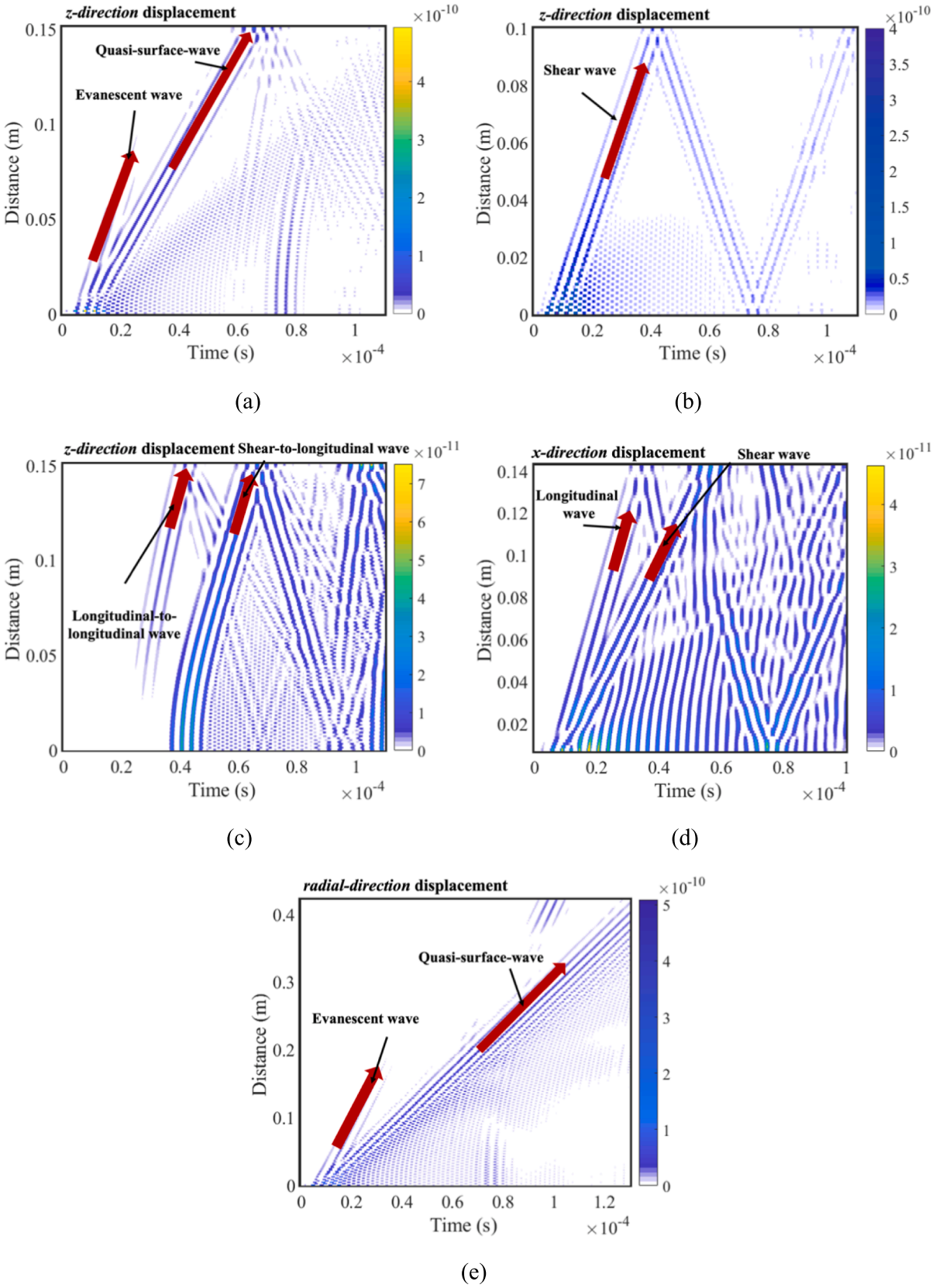

Fig. 5. FE simulated wave propagation trajectory on (a) Path A (*z*-direction displacement), (b) Path B (*z*-direction displacement), and (c) Path C (*z*-direction displacement), (d) Path D (*x*-direction displacement), (e) Path E (radial-direction displacement).

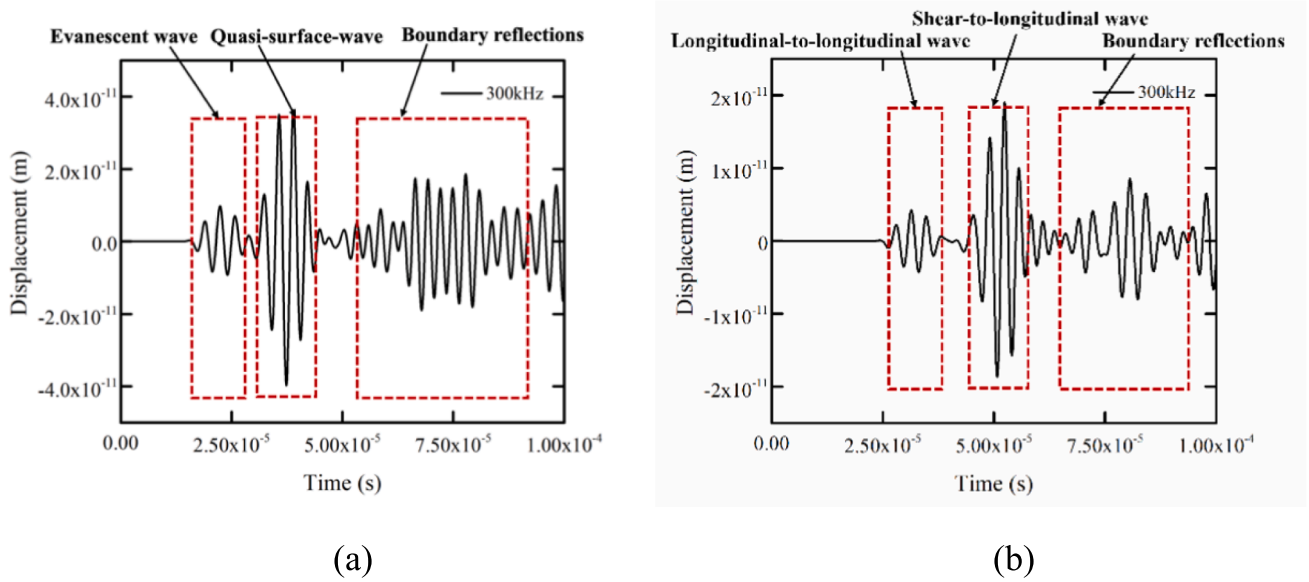

Fig. 6. FE simulated time-domain signals captured at: (a) top surface and (b) bottom surface in terms z direction displacement.

To achieve a quantified estimation of the transducer network performance, the concept of the horizontal dilution of precision (HDOP) [45] is employed. HDOP evaluates the localization performance of different transducer network configurations by mapping the measurement error into a so-called positioning error. Some intermediate variables are necessary to calculate the HDOP as.

$$L_i = \frac{\boldsymbol{r}_i - \boldsymbol{r}_s}{|\boldsymbol{r}_i - \boldsymbol{r}_s|}; \boldsymbol{G} = \begin{bmatrix} -L_1^T & 1 \\ -L_2^T & 1 \\ \vdots & 1 \\ -L_i^T & 1 \end{bmatrix}; \boldsymbol{A} = \left(\boldsymbol{G}^T \boldsymbol{G}\right)^{-1} \tag{18}$$

where vectors $\boldsymbol{r}_i$ and $\boldsymbol{r}_s$ denote the locations of the sensors and the damage; L_i is a unit vector along with the line-of-slight from damage to the sensor i, $(i = 1,\ldots,n)$. Finally, the value of HDOP can be calculated as.

$$HDOP = \sqrt{A_{11} + A_{22}} \tag{19}$$

where A_{11} and A_{22} are the first two diagonal elements of $\boldsymbol{A}$. Therefore, a smaller HDOP value corresponds to a better transducer network.

4. Numerical validations

Numerical simulations are first carried out to validate the proposed damage localization strategy. Specifically, two typical transducer network configurations are evaluated.

4.1. FE model description

A 3-D FE model is established in Abaqus/Explicit as sketched in Fig. 8 (a). The main parameters used in the simulations include: inner and outer radii of the hollow cylinder: 50 mm and 100 mm, respectively; Young's modulus of 71 GPa, mass density of 2700 kg/m3 and Poisson's ratio of 0.33. In this simulation, only the first arrivals in the signals are used for damage localization and the length of 300 mm is enough to discern the first arrivals in the repsonse signals. Therefore, the signals reflected from the boundaries do not affect the proposed method. The excitation is a prescribed displacement in the z direction with a 5-cycle tone burst signal at 300 kHz to mimic a surface-mounted actuator. Similarly, the displacements in the z direction at different sensing locations are extracted as the sensor outputs. A semicircle seam crack with a radius of 10 mm is introduced as a structural damage, which is located at the mid-span of the cylinder over its outer surface. The maximum mesh size used in the FE model is 1 mm, which ensures more than 10 elements per shortest wavelength under consideration. Two transducer network configurations, shown in Fig. 8(b) and (c), are considered, which are mapped to the outer surface of the cylinder. Transducers on the inner surface are correspondingly installed as illustrated in Fig. 8(d) and (e). According to the proposed damage localization strategy, the transducers on the outer surface are switched on in turn to provide the excitation whilst the sensors on the inner surfaces capture the wave responses. In each run, the signal is recorded during a total duration of 115 μs with a sampling frequency of 10 MHz.

4.2. Signal processing and feature extraction

Response signals before and after the introduction of the crack are captured which are referred to as the intact and crack status, respectively. The proposed method is in line with the philosophy of structural health monitoring. In practical applications, measurement of guided waves can be carried out on scheduled time interval. In two sequential tests, the former can serve as the baseline while the latter produces the measurement signals. If damage occurs between the two tests, the proposed method can be used for its localization. Typically, when A3 is used as actuator in Configuration A, typical responses from S3 on the inner surface are shown in Fig. 9(a). The black and red lines represent signals at the intact and cracked status, respectively, which show significant differences. By subtracting the intact signals from the crack signals, the damage-scattering signals can be obtained as indicated by blue lines in both figures.

It should be noted that a comprehensive SHM paradigm should usually conduct a damage-detection process prior to further damage localization or even damage identification. If no damage occurs between two subsequent measurements, the corresponding difference signals are usually very weak. In this case, it is reasonable to conclude that no defect occurs in the structure and it is not necessary to continue with localization. Having said that, we would like to emphasize that the main focus of this work is to propose a damage localization method based on the wave propagation characteristics in TWHCs. A more comprehensive SHM method, which combines damage detection, localization and more advanced functions will be considered in future work.

A complex Morlet wavelet transform is applied to extract the time-of-arrival of the damage-scattered signals. With the excitation position at S3 in Configuration A, the normalized wavelet coefficients of the

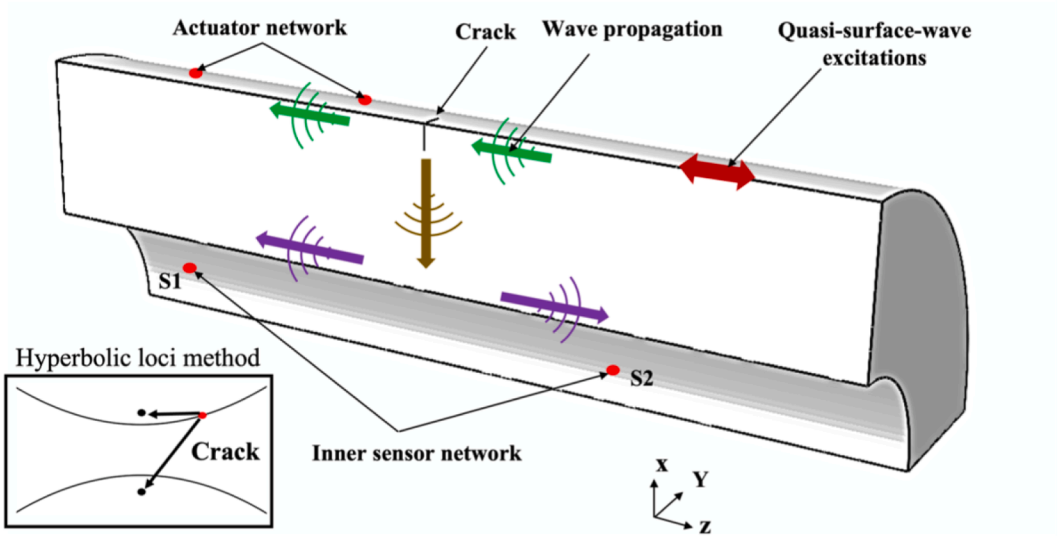

(a)

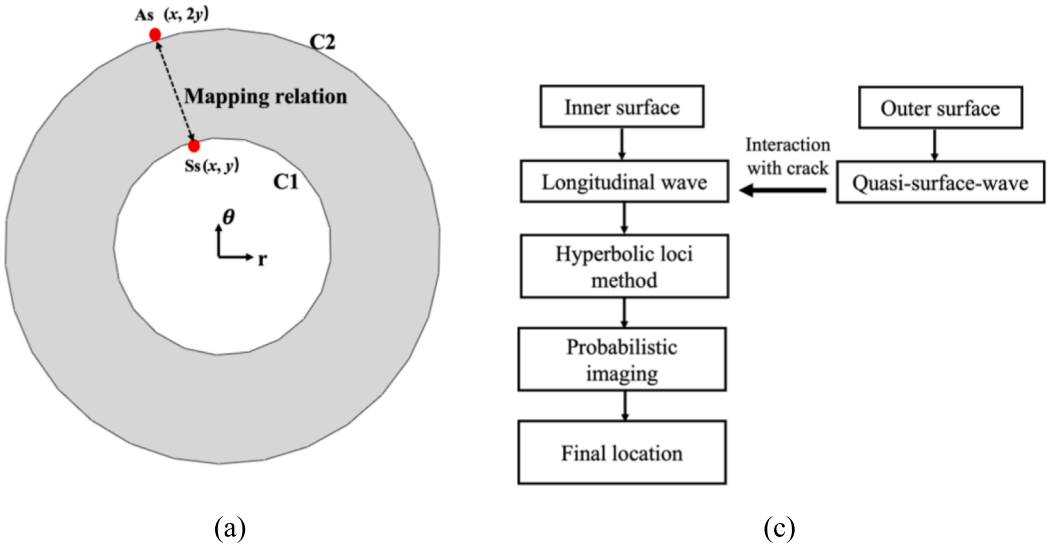

(a) (c)

Fig. 7. (a) Sketch of the 3D FE hollow cylinder and damage, (b) Mapping relation between coordinate C1 and C2, (c) Sketch of the localization strategy.

damage-scattered signals at different sensor positions are calculated at a center frequency of 300 kHz as shown in Fig. 9(b). Considering the signal-to-noise ratio, four largest coefficients out of the five are chosen at the inner surface. As different actuator-receiver paths show different sensitivities to damage, an essential step is to normalize the wavelet coefficients. The magnitude of the normalized wavelet coefficient relates to the number of changes in the received signal caused by the damage. Meanwhile, the normalization process ensures that all actuator-receiver paths provide sufficient damage information in the damage imaging process. The duration of the response signals is truncated to 100 μs to reduce the influence of reflections from the structural boundary.

4.3. Localization and sensor network comparisons

The effectiveness of the proposed localization strategy and that of the transducer networks are validated. For Configuration A, with the extracted temporal information from the wavelet transform, the damage image is reconstructed with the hyperbolic loci method on the inner surface as shown in Fig. 10(a).

Following the same procedure, the damage localization results for Configuration B are shown in Fig. 10(b). Both results show that the inner strategy produce acceptable localization results. Specifically, the localization error (the distance between the actual damage center to the identified damage center indicated by the highest P_{inner}) are 14 and 8 mm respectively for the two cases.

Two more cases (I and II) with different defect sizes and positions are considered with sensor Configuration B to assess the proposed network. For the first case (Case I), the damage center location is (0.13 m, −0.019 m) and the radius of the defect is 13 mm, as shown in Fig. 11(a). The identified damage location is (0.1238 m, −0.0129 m) and the localization error is 9 mm, are shown in Fig. 11(b). For the second case, the damage center location is (0.16 m, 0.039 m) and the radius of the defect is 15 mm, as shown in Fig. 12(a). The proposed localization method yields an identified damage location (0.1564 m, 0.04864 m) with an error of 10 mm as shown in Fig. 12(b).

It is worth noting the damage size mainly affect the amplitude of the scattering waves rather than their termporal information. Since the proposed method leverages the temporal information from the difference signals for damage localization, it is barely affected by the size of the damage in principle. However, in practical applications, when the

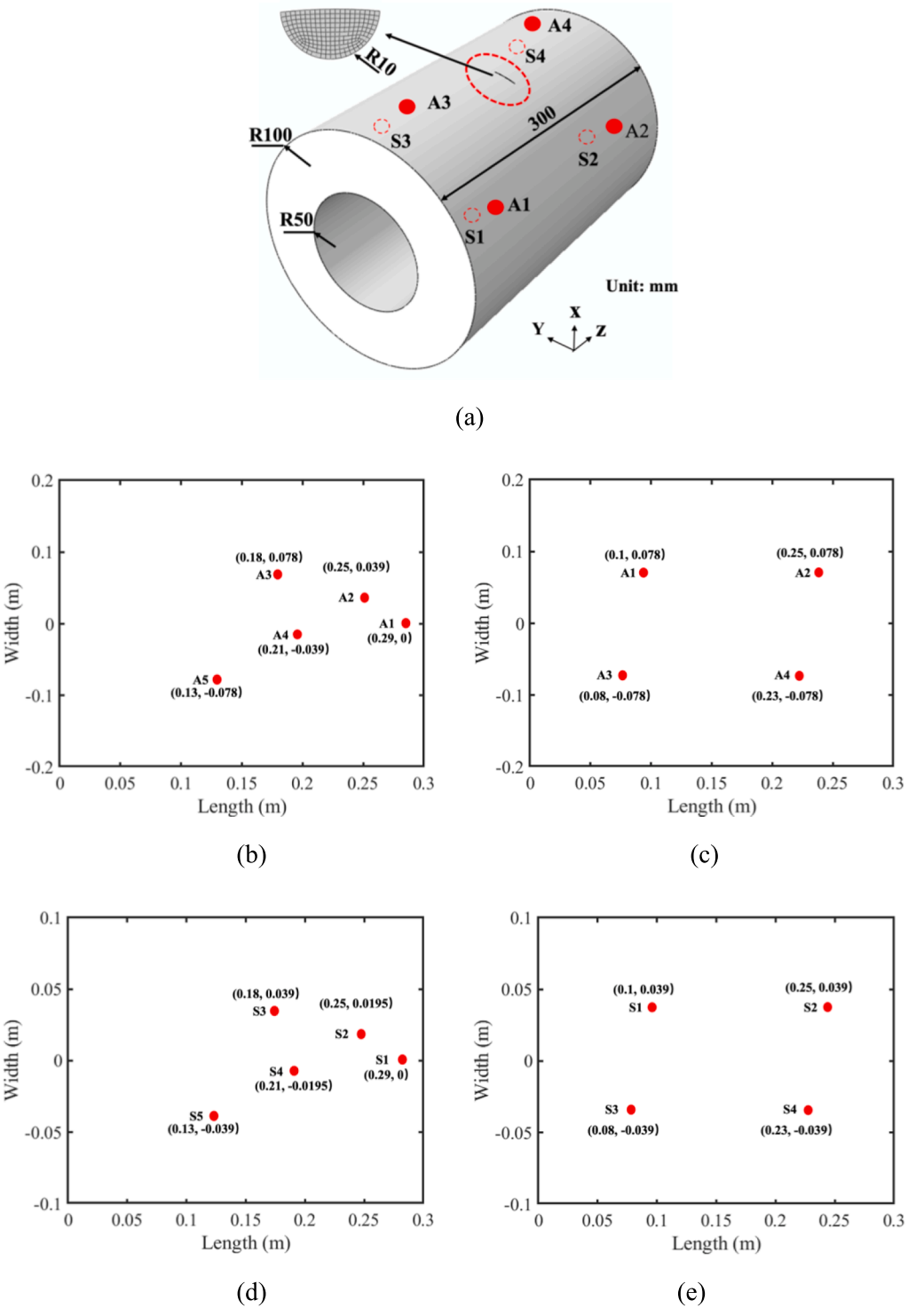

Fig. 8. (a) Sketch of the 3D FE hollow cylinder and damage. Two actuator sensor network arrangements over the outer surface: (b) Configuration A and (c) Configuration B. Two transducer sensor network arrangements over the inner surface: (d) Configuration A and (e) Configuration B.

damage is small, the damage scattering waves will be very weak and prone to measurement noise. In that case, the localization accuracy of the proposed method might be compromised.

The performance of the transducer networks are then evaluated. For any given damage location, the corresponding HDOP can be calculated. Consequently, the HDOP distribution can be constructed as shown in Fig. 13 in relation to the proposed transducer network. It can be seen the HDOP at the corner of Configuration A is extremely large in Fig. 13(a), which indicates a low damage localization accuracy at that area. Therefore, Configuration B outperforms Configuration A. In addition, for the specific damage case, the corresponding HDOPs are 1.3155 and 1.0058 for Configurations A and B respectively. This also indicates that Configuration B is better than Configuration A as evidenced by the lower localization error associated with the synthesized strategy. Therefore, Configuration B will be used in the design of the transducer network used in experiments.

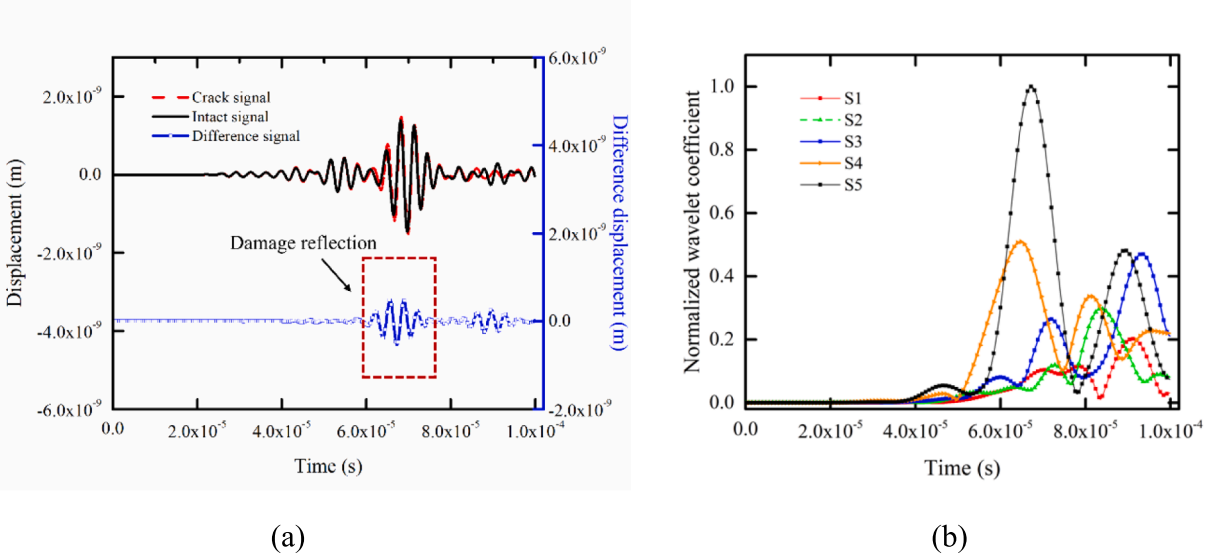

Fig. 9. FE simulated response signals when excitation is applied at A3 in Configuration A: (a) time-domain signals at S3, (b) the wavelet coefficients of the damage-scattered signals at the sensors on the inner surfaces.

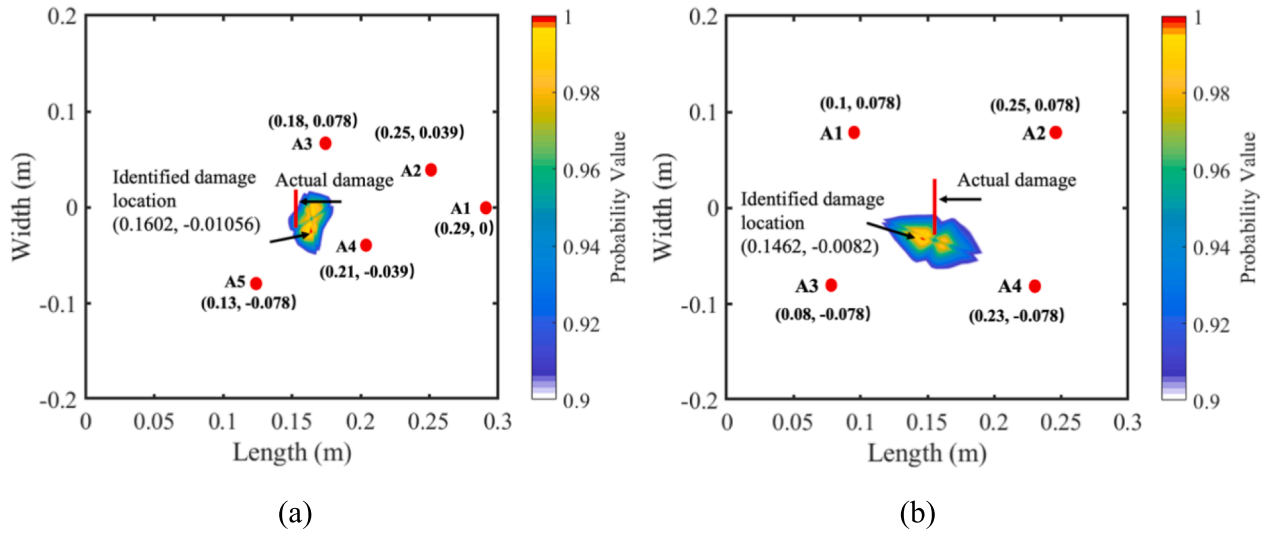

Fig. 10. Damage localization results with (a) Configuration A and (b) Configuration B.

5. Experimental validation

5.1. Experimental setup

Experiments are carried out to further validate the proposed localization strategy with an aluminum hollow cylinder of a total length of 500 mm, an inner and outer diameters of 100 mm and 200 mm (see Fig. 14). Eight circular piezoelectric wafer transducers (PZT), 0.5 mm thick and 6 mm in diameter, are bonded onto the outer and inner surfaces of the hollow cylinder with instant glue. The measurement system is shown in Fig. 14. A controller generates a tone burst excitation signal through the KEYSIGHT 33500B Waveform Generator. The signal is amplified by the GA-2500A Gated RF amplifier to drive the PZT actuator. The generated waves are captured by the PZT sensors and recorded by the NI PXIe-5105 data acquisition module. Finally, the response signals are stored and processed by the controller.

Guided by the FE analyzes, four PZTs are mounted on the outer surface of structure and the other four on the inner surface. The 200 V 5-cycle Hann-windowed tone burst signal centered at 300 kHz is used. The signals captured by sensors are averaged by 100 measurements to reduce the adverse influence of the measurement noise. A notch, roughly 20 mm long, 1 mm wide and 3 mm deep is fabricated to mimic a structural damage as shown in Fig. 14.

5.2. Feature extraction from the measured responses

Similar to the FE simulations, Fig. 15(a) presents the response signals in the intact and crack status as well as the corresponding damage-scattered signals at S3 when A2 is activated for excitation. The wave packets associated with the damage-scattered signals can be clearly observed. After complex Morlet wavelet transform, the time-of-arrival of the damage-scattering signals are extracted. The normalized wavelet coefficients of the damage-scattering signals at different sensor positions are calculated and shown in Fig. 15(b). Similarly, three out of four of damage-scattered signals, considered to be the most representative in terms of amplitude, are used in the damage localizaton algorithm.

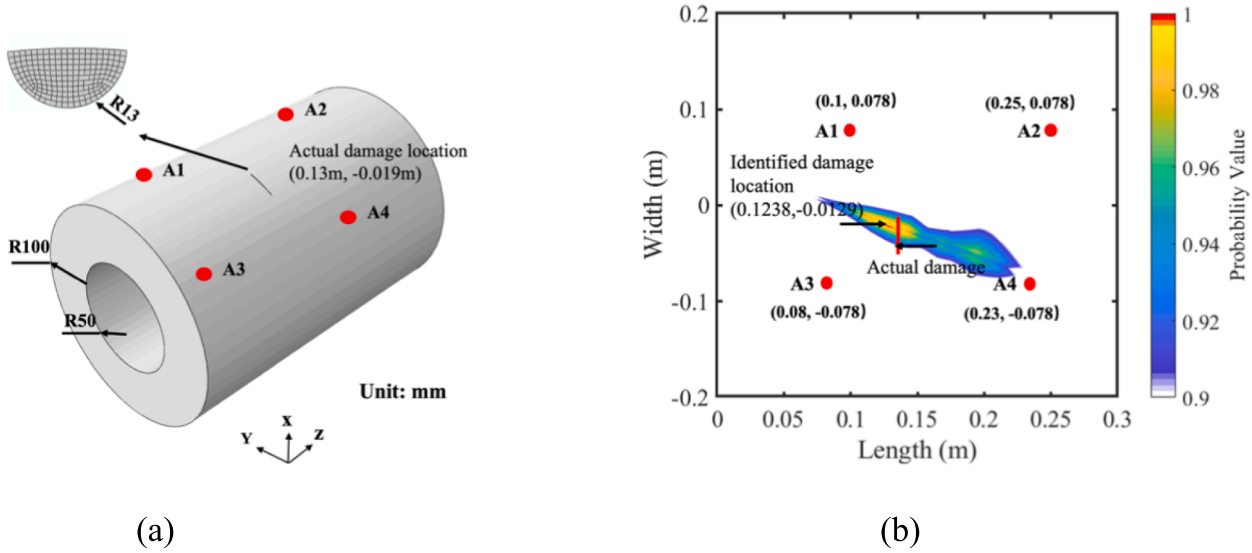

Fig. 11. (a) Sketch of the 3D FE hollow cylinder and damage and (b) damage localization result in Case I.

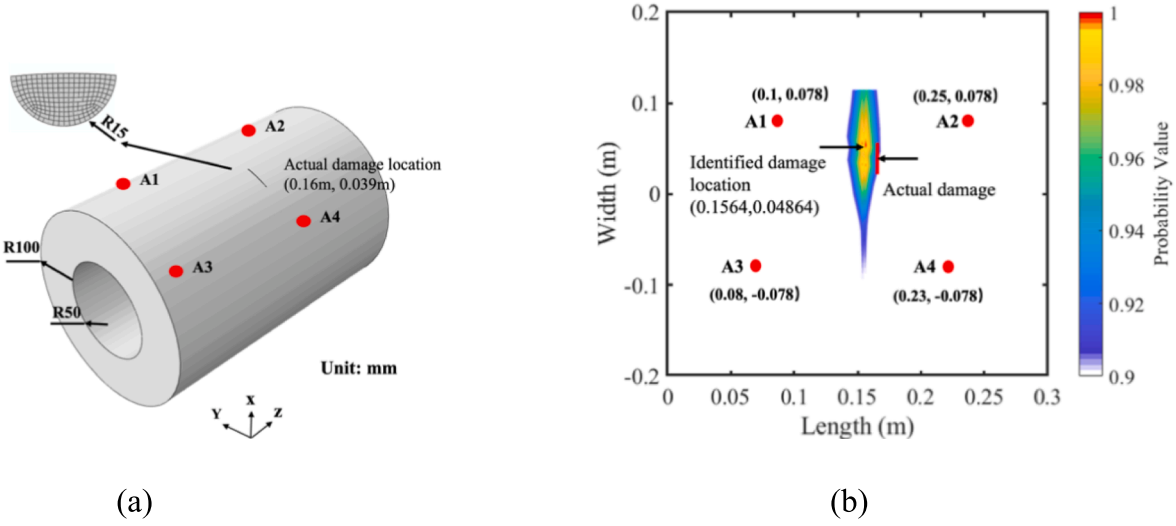

Fig. 12. (a) Sketch of the 3D FE hollow cylinder and damage and (b) damage localization result in Case II.

5.3. Damage localization results

With the extracted temporal information from the damage-scattered signals, damage image is reconstructed for the proposed damage localization strategy in Fig. 16. The identified damage localization is (0.1446 m, 0.00242 m) as indicated by the position of the highest value of P_{inner} and the localization error is 5 mm with respect to the actual damage location at (0.15 m, 0). This further confirms the efficacy of the proposed method.

6. Conclusions

In this work, the wave propagation in a TWHC is investigated from both theoretical and numerical perspectives. Based on the acquired understanding, a damage localization strategy is proposed using inner surface sensing. Finite element analyses are first carried out to validate the proposed method and to assess the influence of the transducer network layout. Experimental validations are finally conducted.

Studies reveal that, an outer surface excitation generates dominant quasi-surface-waves on the outer surface alongside the shear bulk waves propagating through the wall thickness direction in a TWHC. Reaching the inner surface, the bulk waves are converted into longitudinal waves to propagate along the inner surface rather than quasi-surface-waves. Capitalizing on this understanding, damage localization is successfully achieved by using hyperbolic loci method through inner surface sensing, as confirmed by both FE simulations and experiments. With a proper sensor network layout guided by HDOP analysis, the synthesized sensing strategy entails enhanced localization accuracy.

The reported findings are expected to fill the gap between thin-walled structures and infinitely large half-space elastic media, specific to TWHCs. The reported mode conversion phenomena might pave the way for further exploration and application of damage detection and localization in thick-walled structures. The proposed damage localization strategy as well the evaluation method for the transducer network design may also offer useful guidance for practical engineering applications such as the monitoring of train axles.

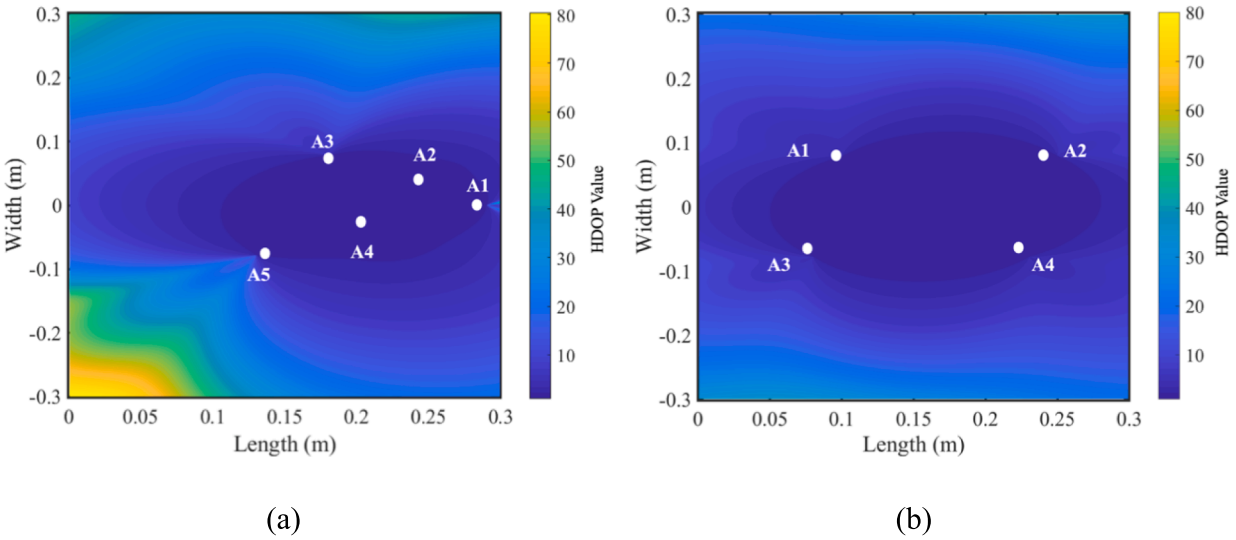

Fig. 13. HDOP in (a) Configuration A and (b) Configuration B.

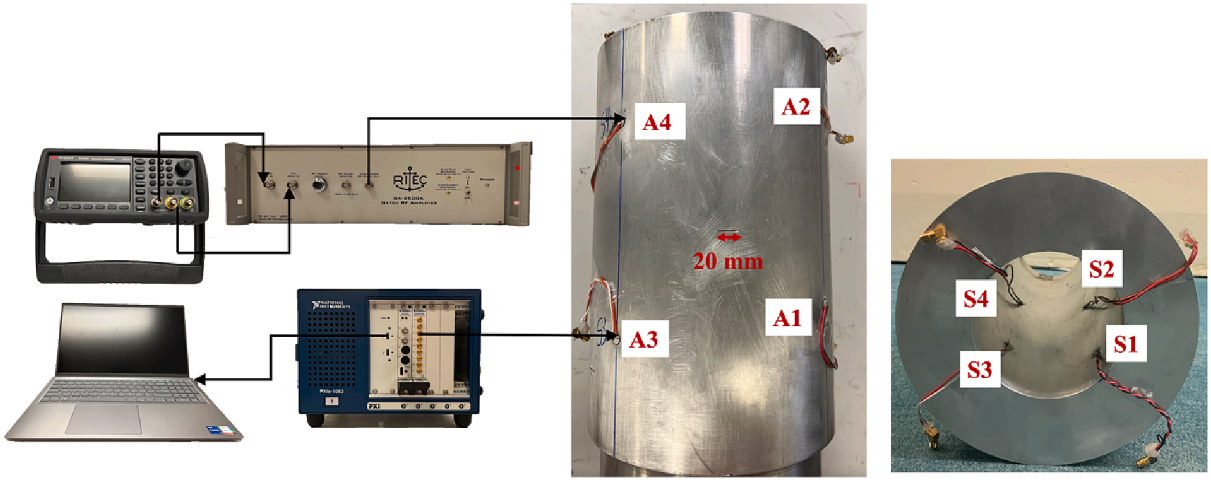

Fig. 14. Experimental setup.

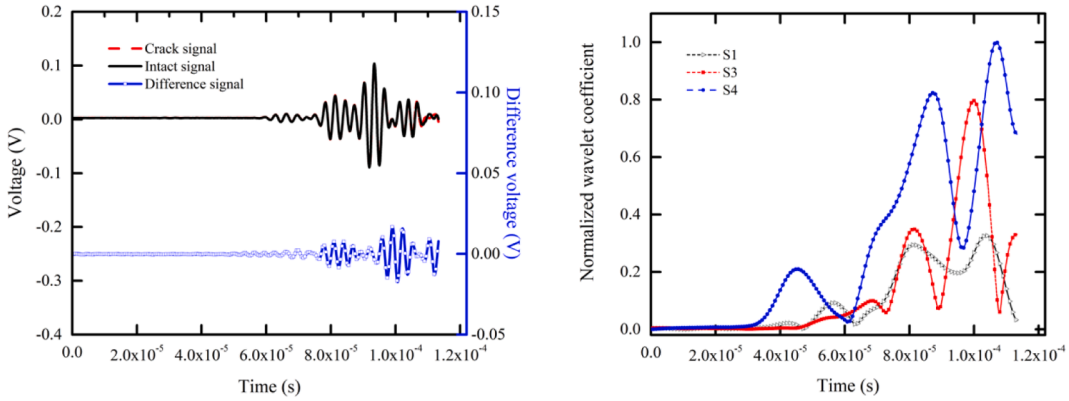

Fig. 15. Experimentally measured response signals activated at A2: (a) time-domain signals at S3, (b) the wavelet coefficients of the damage-scattered signals at the sensors on the inner surfaces.

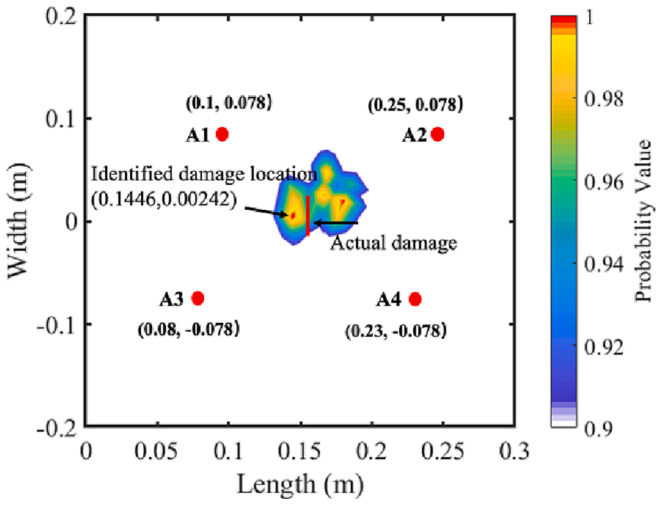

Fig. 16. Experimental damage localization results: damage image obtained from the inner strategy.

Declaration of Competing Interest

The authors declare that they have no known competing financial interests or personal relationships that could have appeared to influence the work reported in this paper.

Data availability

Data will be made available on request.

Acknowledgments

This work was supported by the Research Grants Council of Hong Kong Special Administrative Region [PolyU 152013/21E]; the National Natural Science Foundations of China through SHENG project [Polish-Chinese Funding Initiative, 51961135302]; Research Fund of State Key Laboratory of Mechanics and Control of Mechanical Structures [Nanjing University of Aeronautics and Astronautics, China. Grant No. MCMS-E-0520K01]; the Natural Science Foundation of Shanghai [22ZR1462700]; the Fundamental Research Funds for the Central Universities; and the Innovation and Technology Commission of the HKSAR Government to the Hong Kong Branch of National Rail Transit Electrification and Automation Engineering Technology Research Center.

References

[1] K. Makino, S. Biwa, Influence of axle–wheel interface on ultrasonic testing of fatigue cracks in wheelset, Ultrasonics 53 (1) (2013) 239–248.
[2] A. Cavuto, M. Martarelli, G. Pandarese, G. Revel, E. Tomasini, Experimental investigation by laser ultrasonics for high speed train axle diagnostics, Ultrasonics 55 (2015) 48–57.
[3] C. Mineo, D. Cerniglia, A. Pantano, Numerical study for a new methodology of flaws detection in train axles, Ultrasonics 54 (3) (2014) 841–849.
[4] C.R. Farrar, K. Worden, An introduction to structural health monitoring, Philos. Trans. R. Soc. A Math. Phys. Eng. Sci. 365 (1851) (2007) 303–315.
[5] J. Man, et al., GCG: Graph Convolutional network and gated recurrent unit method for high-speed train axle temperature forecasting, Mech. Syst. Sig. Process. 163 (2022), 108102.
[6] G. Niu, L. Xiong, X. Qin, M. Pecht, Fault detection isolation and diagnosis of multi-axle speed sensors for high-speed trains, Mech. Syst. Sig. Process. 131 (2019) 183–198.
[7] P. Seventekidis, D. Giagopoulos, A. Arailopoulos, O. Markogiannaki, Structural Health Monitoring using deep learning with optimal finite element model generated data, Mech. Syst. Sig. Process. 145 (2020), 106972.
[8] S. Shan, Z. Liu, L. Cheng, Y. Pan, Metamaterial-enhanced coda wave interferometry with customized artificial frequency-space boundaries for the detection of weak structural damage, Mech. Syst. Sig. Process. 174 (2022), 109131.
[9] H. Miao, F. Li, Shear horizontal wave transducers for structural health monitoring and nondestructive testing: A review, Ultrasonics 114 (2021), 106355.
[10] Q. Huan, M. Chen, F. Li, Long-distance structural health monitoring of buried pipes using pitch-catch T (0, 1) wave piezoelectric ring array transducers, Ultrasonics 106 (2020), 106162.
[11] R. Gorgin, Y. Luo, Z. Wu, Environmental and operational conditions effects on Lamb wave based structural health monitoring systems: A review, Ultrasonics 105 (2020), 106114.
[12] D.C. Gazis, Three-dimensional investigation of the propagation of waves in hollow circular cylinders. I. Analytical foundation, J. Acoust. Soc. Am. 31 (5) (1959) 568–573.
[13] D.C. Gazis, Three-dimensional investigation of the propagation of waves in hollow circular cylinders. II. numerical results, J. Acoust. Soc. Am. 31 (5) (1959) 573–578.
[14] D. Bancroft, The velocity of longitudinal waves in cylindrical bars, Phys. Rev. 59 (7) (1941) 588–593.
[15] K. Murai, D. Kong, H. Tamura, and M. Aoyagi, "Hollow Cylindrical Linear Stator Vibrator Using a Traveling Wave of Longitudinal Axisymmetric Vibration Mode," *Available at SSRN 4048918*.
[16] W. Li, Z. Lan, N. Hu, M. Deng, Modeling and simulation of backward combined harmonic generation induced by one-way mixing of longitudinal ultrasonic guided waves in a circular pipe, Ultrasonics 113 (2021), 106356.
[17] A. Darinskii, A. Shuvalov, O. Poncelet, A. Kutsenko, Bulk longitudinal wave reflection/transmission in periodic piezoelectric structures with metallized interfaces, Ultrasonics 63 (2015) 118–125.
[18] S. Akbarov, T. Kepceler, M.M. Egilmez, Torsional wave dispersion in a finitely pre-strained hollow sandwich circular cylinder, J. Sound Vib. 330 (18–19) (2011) 4519–4537.
[19] M. Castaings, C. Bacon, Finite element modeling of torsional wave modes along pipes with absorbing materials, J. Acoust. Soc. Am. 119 (6) (2006) 3741–3751.
[20] G. Okudan, C. Xu, H. Danawe, S. Tol, D. Ozevin, Controlling the thickness dependence of torsional wave mode in pipe-like structures with the gradient-index phononic crystal lens, Ultrasonics 124 (2022), 106728.
[21] F. Honarvar, E. Enjilela, A.N. Sinclair, S.A. Mirnezami, Wave propagation in transversely isotropic cylinders, Int. J. Solids Struct. 44 (16) (2007) 5236–5246.
[22] D.M. Joglekar, M. Mitra, Analysis of flexural wave propagation through beams with a breathing crack using wavelet spectral finite element method, Mech. Syst. Sig. Process. 76 (2016) 576–591.
[23] E. Leinov, M.J. Lowe, P. Cawley, Investigation of guided wave propagation and attenuation in pipe buried in sand, J. Sound Vib. 347 (2015) 96–114.
[24] R. Sanderson, D.A. Hutchins, D.R. Billson, P. Mudge, The investigation of guided wave propagation around a pipe bend using an analytical modeling approach, J. Acoust. Soc. Am. 133 (3) (2013) 1404–1414.
[25] J. Rose, J. Li, X. Zhao, M. Quarry, Ultrasonic guided wave flexural mode tuning for limited access pipe inspection, in: AIP Conference Proceedings, vol. 557, no. 1, American Institute of Physics, 2001, pp. 164–171.
[26] C. Bao, L. Gu, S. Zhang, Q. Wang, Finite Element Analysis of Ultrasonic Guided Wave Propagation and Damage Detection in Complex Pipeline, in: Intelligent Equipment, Robots, Springer, and Vehicles, 2021, pp. 617–626.
[27] M. Eybpoosh, M. Berges, H.Y. Noh, An energy-based sparse representation of ultrasonic guided-waves for online damage detection of pipelines under varying environmental and operational conditions, Mech. Syst. Sig. Process. 82 (2017) 260–278.
[28] M. Gresil, A. Poohsai, N. Chandarana, Guided wave propagation and damage detection in composite pipes using piezoelectric sensors, Procedia Eng. 188 (2017) 148–155.
[29] Z. Song, X. Qi, Z. Liu, H. Ma, Experimental study of guided wave propagation and damage detection in large diameter pipe filled by different fluids, NDT and E Int. 93 (2018) 78–85.
[30] H. Yun, W. Zhang, Damage detection based on the propagation of longitudinal guided wave in a bimetal composite pipe, Theor. Appl. Mech. Lett. 1 (2) (2011), 021004.
[31] S.M. Hasheminejad, M. Rajabi, Acoustic scattering characteristics of a thick-walled orthotropic cylindrical shell at oblique incidence, Ultrasonics 47 (1–4) (2007) 32–48.
[32] F. Li, X. Sun, J. Qiu, L. Zhou, H. Li, G. Meng, Guided wave propagation in high-speed train axle and damage detection based on wave mode conversion, Struct. Control Health Monit. 22 (9) (2015) 1133–1147.
[33] A. Ziaja, L.i. Cheng, Z. Su, P. Packo, L. Pieczonka, T. Uhl, W. Staszewski, Thick hollow cylindrical waveguides: A theoretical, numerical and experimental study, J. Sound Vib. 350 (2015) 73–90.
[34] A. Ziaja-Sujdak and L. Cheng, "A guided wave-based inspection methodology for high speed train hollow axles," in *8th European Workshop on Structural Health Monitoring, EWSHM 2016*, 2016: NDT. net, pp. 2190-2199.
[35] J.J. Ditri, Utilization of guided elastic waves for the characterization of circumferential cracks in hollow cylinders, J. Acoust. Soc. Am. 96 (6) (1994) 3769–3775.
[36] A. Ziaja-Sujdak, L. Cheng, R. Radecki, W.J. Staszewski, Near-field wave enhancement and 'quasi-surface'longitudinal waves in a segmented thick-walled hollow cylindrical waveguide, Struct. Health Monit. 17 (2) (2018) 346–362.
[37] C. Hu, B. Yang, B. Xiao, F.-Z. Xuan, Y. Xiang, Damage localization in pressure vessel using guided wave-based techniques: Optimizing the sensor array configuration to mitigate nozzle effects, Appl. Acoust. 185 (2022), 108393.
[38] B. Yang, et al., Damage localization in hydrogen storage vessel by guided waves based on a real-time monitoring system, Int. J. Hydrogen Energy 44 (40) (2019) 22740–22751.
[39] B. Shi, M. Cao, Z. Wang, W. Ostachowicz, A directional continuous wavelet transform of mode shape for line-type damage detection in plate-type structures, Mech. Syst. Sig. Process. 167 (2022), 108510.

[40] J.E. Greenspon, Flexural vibrations of a thick-walled circular cylinder according to the exact theory of elasticity, Journal of the Aerospace Sciences 27 (1) (1960) 37–40.
[41] J. Kudlička, Dispersion of torsional waves in a thick-walled transversely isotropic circular cylinder of infinite length, J. Sound Vib. 294 (1–2) (2006) 368–373.
[42] S.M. Hosseini, M.H. Abolbashari, General analytical solution for elastic radial wave propagation and dynamic analysis of functionally graded thick hollow cylinders subjected to impact loading, Acta Mech. 212 (1-2) (2010) 1–19.
[43] J.L. Rose (Ed.), Ultrasonic Guided Waves in Solid Media, Cambridge University Press, 2014.
[44] J.B. Keller, F.C. Karal Jr, Surface wave excitation and propagation, J. Appl. Phys. 31 (6) (1960) 1039–1046.
[45] A. Melkonyan, D. Akopian, and C. P. Chen, "A sensor placement measure for impact detection in structural health monitoring," in *2009 IEEE International Conference on Systems, Man and Cybernetics*, 2009: IEEE, pp. 3775-3778.